

Morphological analysis for thermodynamics of cavitation collapse near fractal solid wall

Minglei Shan(单鸣雷), Yu Yang(杨雨), Xuefen Kan(阚雪芬), Cheng Yin(殷澄), Qingbang Han(韩庆邦)

Citation: Chin. Phys. B, 2024, 33 (**6**): 064701. DOI: 10.1088/1674-1056/ad3343
Journal homepage: http://cpb.iphy.ac.cn; http://iopscience.iop.org/cpb

What follows is a list of articles you may be interested in

Discussion on interface deformation and liquid breakup mechanism in vapor-liquid two-phase flow

Xiang An(安祥), Bo Dong(董波), Ya-Jin Zhang(张雅瑾), and Xun Zhou(周训)
Chin. Phys. B, 2023, 32 (**9**): 094702. DOI: 10.1088/1674-1056/acc78e

Application of shifted lattice model to 3D compressible lattice Boltzmann method

Hao-Yu Huang(黄好雨), Ke Jin(金科), Kai Li(李凯), and Xiao-Jing Zheng(郑晓静)
Chin. Phys. B, 2023, 32 (**9**): 094701. DOI: 10.1088/1674-1056/acc78d

Improved contact angle measurement in multiphase lattice Boltzmann

Xing-Guo Zhong(钟兴国), Yang-Sha Liu(刘阳莎), Yi-Chen Yao(姚怡辰), Bing He(何冰), and Bing-Hai Wen(闻炳海)
Chin. Phys. B, 2023, 32 (**5**): 054701. DOI: 10.1088/1674-1056/ac9cbd

Hemodynamics of aneurysm intervention with different stents

Peichan Wu(吴锆婵), Yuhan Yan(严妤函), Huan Zhu(朱欢), Juan Shi(施娟), and Zhenqian Chen(陈振乾)
Chin. Phys. B, 2022, 31 (**6**): 064701. DOI: 10.1088/1674-1056/ac5603

Particle captured by a field-modulating vortex through dielectrophoresis force

Bing Yan(严兵), Bo Chen(陈波), Zerui Peng(彭泽瑞), and Yong-Liang Xiong(熊永亮)
Chin. Phys. B, 2022, 31 (**3**): 034703. DOI: 10.1088/1674-1056/ac248a

---

Morphological analysis for thermodynamics of cavitation collapse near fractal solid wall

Minglei Shan(单鸣雷)[1,†], Yu Yang(杨雨)[2,‡], Xuefen Kan(阚雪芬)[3], Cheng Yin(殷澄)[1], and Qingbang Han(韩庆邦)[1]

[1] *Jiangsu Key Laboratory of Power Transmission and Distribution Equipment Technology, Hohai University, Changzhou* 213022, *China*
[2] *College of Information Science and Technology, Nanjing Forestry University, Nanjing* 210000, *China*
[3] *Department of Transportation Engineering, Jiangsu Shipping College, Nantong* 226000, *China*

(Received 21 December 2023; revised manuscript received 13 February 2024; accepted manuscript online 13 March 2024)

A fractal geometric boundary with natural wall features is introduced into a hybrid lattice-Boltzmann-method (LBM) multiphase model. The physical model of cavitation bubble collapse near the irregular geometric wall is established to study the thermodynamic characteristics of the bubble collapse. Due to the lack of periodicity, symmetry, spatial uniformity and obvious correlation in the LBM simulation of the bubble collapse near the fractal wall, the morphological analysis based on Minkowski functional is introduced into the thermodynamic investigation of cavitation bubble so as to analyze and obtain the effective information. The results show that the Minkowski functional method can employed to study the temperature information in complex physical fields hierarchically and quantitatively. The high/low temperature region of the cavitation flow is explored, and thermal effect between irregular and fractal geometric wall and cavitation bubble can be revealed. It illustrates that LBM and morphological analysis complement each other, and morphological analysis can also be used as an optional and potential tool in research field of complex multiphase flows.

Keywords: lattice Boltzmann method, cavitation bubble, morphological analysis

PACS: 47.11.Qr, 47.55.Ca, 47.55.dd, 47.55.dp **DOI:** 10.1088/1674-1056/ad3343

1. Introduction

Cavitation bubble is an excellent aggregation microsystem. The bubble collapses instantly when the internal and external pressure reaches a certain condition, resulting in an instantaneous high temperature about 1900–5200 K and a high pressure above 50 MPa. The temperature change rate can reach 109 K/s to form high intensity shock wave.[1] The intricate dynamics of cavitation collapse have garnered significant attention due to their profound impact on phenomena such as sonoluminescence, hydraulic erosion, and biomedical applications. Despite decades of research, understanding the underlying mechanisms governing cavitation collapse remains a challenging endeavor, particularly in the presence of complex geometries.

Most cavitation applications involve the interaction of cavitation bubble with solid surfaces. Many scholars have devoted to using numerical methods to study the collapse process and interaction mechanism of cavitation bubble near solid walls with regular geometric characteristics, such as flat wall, curved wall, and perforated wall.[2–6] Among many numerical research methods, the lattice Boltzmann method (LBM) based on mesoscopic perspective is prominent in describing thermodynamics of bubble collapse near a wall. Yang *et al.* firstly used the improved thermal lattice model of double distribution function (DDF) to construct a thermodynamic model of collapsing cavitation bubble near a flat wall. The feasibility of establishing the thermodynamic lattice Boltzmann (LB) model is verified by experimental data and numerical calculation.[7,8] On the basis, Liu *et al.*[9] adopted the improve DDF LBM to simulate the evolution process of cavitation bubble under non-isothermal conditions. The thermodynamic mechanism of the bubble growth and collapse under three boundary conditions of infinite domain, flat wall, and convex wall is studied. Peng *et al.*[10] extended the thermodynamic model of single bubble and double bubble collapsing near a rigid wall based on the DDF thermal lattice model, and reproduced the thermodynamic evolution process of cavitation bubble and the corrosion inhibition effect of the rigid wall. The above-mentioned research results illustrate that the mesoscopic LBM can efficiently integrate direct physical modeling, automatic evolution of multiphase flow, thermodynamic description, and construction of complex boundary wall, which make it possible to establish a model of bubble collapse near the wall integrating hydrodynamics and thermodynamics. With the extensive application and in-depth research of LBM, the LB model coupled with multiple particle distribution functions and the hybrid model coupled with macro numerical modeling methods (such as the finite element method, the finite difference method, and the finite volume method) came into being.[11–14] It provides a reference direction for the construction of stable, efficient and accurate numerical model of cavitation bubble. However, although the above-mentioned research involves the mechanism between the bubble collapse and complex walls, the geomet-

[†]Corresponding author. E-mail: shanming2003@126.com
[‡]Corresponding author. E-mail: yang1996@njfu.edu.cn

© 2024 Chinese Physical Society and IOP Publishing Ltd

ric solid wall constructed is mostly regular, which is still not enough to reveal the collapse mechanism of a bubble in real physical environments.

Different models of cavitation bubble collapse near a wall can be established by using the LBM numerical method. According to the geometrical characteristics of the wall surface, the collapse process of the bubble can be divided into symmetric and asymmetric collapse. The early studies[15–18] have shown that the simulated physical field is simple, intuitive and symmetrical when the bubble collapses near a flat wall. The interaction between fluid–fluid/fluid–solid and the thermodynamic process can be effectively and conveniently described only by LBM. However, when the wall surface is no longer flat but has irregular complex geometry, such as the leaf surface, the cell surface, the crack surface of metal and rock, which have certain randomness and present the features of fractal geometry, the geometrical features of solid surface are not negligible when cavitation occurs on the above-mentioned similar surfaces. It will increase the difficulty of studying the interaction mechanism between the bubble and the solid wall. For the solid wall with complex irregular geometric characteristics, the collapse process lacks periodicity, symmetry, spatial uniformity and obvious correlation. Therefore, there is an urgent need for an effective tool that can reduce a large amount spatial information to a limited number of relevant parameters, which is able to extract effective information from the collapse process of cavitation bubble near the complex wall.

Morphological analysis was developed on the basis of the phase space description method of statistical physics. It originated from the geometrical study of the permeability of porous media and developed into a common image processing and analysis technology later.[19,20] The effective information can be analyzed and obtained from complex physical fields by using morphological analysis methods. In recent years, the morphological analysis of Minkowski functional has been successfully applied to the study of complex multiphase flows. For example, Gan *et al.*[21] introduced rheology and Minkowski functional to study non-isothermal phase separation, and analyzed the influence of temperature field on phase morphology and separation velocities. Xu *et al.*[22] conducted a detailed review and simulation verification of the Minkowski functional morphology analysis method in phase space. Cavitation, as a typical multiphase flow system, can also introduce Minkowski functional morphology parameters to quantitatively describe the physical quantities and morphological characteristics of cavitation bubble collapse process as a whole.

In this paper, a hybrid thermal LB model is adopted to investigate the thermodynamic characteristic of cavitation bubble collapse near the fractal solid wall. Meantime, the morphological phase space analysis method of Minkowski functional is used to extract the characteristic behavior of the results of discrete LBM simulation. The information in complex physical field is studied hierarchically and quantitatively from two perspectives. The micro mechanism of the interaction between irregular and complex geometric wall and cavitation bubble is revealed. The rest of the paper is organized as follows: The hybrid thermal lattice Boltzmann model and the morphological measures are introduced in Sections 2 and 3, respectively. The numerical investigation of cavitation bubble collapse near the fractal wall is performed in Section 4. A brief conclusion is given in Section 5.

2. Hybrid thermal model

The pseudopotential model is adopted to simulate the flow field. By using the multiple-relaxation-time collision operator, the lattice Boltzmann extension equation, which governs the evolution of the density distribution functions, can be written as[23,24]

$$\begin{aligned} &f_\alpha(\boldsymbol{x}+\boldsymbol{e}_\alpha\Delta t, t+\Delta t) - f_\alpha(\boldsymbol{x},t) \\ &= -\boldsymbol{M}^{-1}\boldsymbol{\Lambda}\boldsymbol{M}(f_\alpha(\boldsymbol{x},t) - f_\alpha^{\mathrm{eq}}(\boldsymbol{x},t)) + \Delta t S', \end{aligned} \tag{1}$$

where $f_\alpha(x,t)$ is the density distribution function at the lattice site $\boldsymbol{x}$ and time t along α directions, $f_\alpha^{\mathrm{eq}}(\boldsymbol{x},t)$ is the equilibrium distribution function, and $\Delta t S'$ is the external force term in the velocity space. Δx and Δt are the lattice space and time step, respectively. The lattice speed $c = \Delta x/\Delta t = 1$ and the lattice sound speed $c_{\mathrm{s}} = 1/\sqrt{3}$.[25] In this study, the standard D2Q9 discrete velocity model is employed, and $\boldsymbol{e}_\alpha$ is the discrete velocities, where $\alpha = 0, 1, \ldots, 8$. The diagonal matrix $\boldsymbol{\Lambda}$ is given as

$$\boldsymbol{\Lambda} = \mathrm{diag}(\tau_\rho^{-1}, \tau_{\mathrm{e}}^{-1}, \tau_\zeta^{-1}, \tau_j^{-1}, \tau_{\mathrm{q}}^{-1}, \tau_j^{-1}, \tau_{\mathrm{q}}^{-1}, \tau_{\mathrm{v}}^{-1}, \tau_{\mathrm{v}}^{-1}), \tag{2}$$

where the elements are the relaxation time factors for different moments. The kinematic viscosities are $\nu = (1/\tau_{\mathrm{v}} - 0.5)c_{\mathrm{s}}^2\Delta t$. Here the relaxation times are chosen as $\tau_\rho = \tau_j = 1$, $\tau_{\mathrm{e}} = \tau_\zeta = 1.25$, and $\tau_{\mathrm{q}} = 1/1.1$.

$\boldsymbol{M}$ is the non-orthogonal transformation matrix,[1]

$$\boldsymbol{M} = \begin{bmatrix} 1 & 1 & 1 & 1 & 1 & 1 & 1 & 1 & 1 \\ -4 & -1 & -1 & -1 & -1 & -1 & 2 & 2 & 2 \\ 4 & -2 & -2 & -2 & -2 & 1 & 1 & 1 & 1 \\ 0 & 1 & 0 & -1 & 0 & 1 & -1 & -1 & 1 \\ 0 & -2 & 0 & 2 & 0 & 1 & -1 & -1 & 1 \\ 0 & 0 & 1 & 0 & -1 & 1 & 1 & -1 & -1 \\ 0 & 0 & -2 & 0 & 2 & 1 & 1 & -1 & -1 \\ 0 & 1 & -1 & 1 & -1 & 0 & 0 & 0 & 0 \\ 0 & 0 & 0 & 0 & 0 & 1 & -1 & 1 & -1 \end{bmatrix}. \tag{3}$$

Using the transformation matrix $\boldsymbol{M}$, Eq. (1) can be transformed to[26,27]

$$\boldsymbol{m}^* = \boldsymbol{m} - \boldsymbol{\Lambda}(\boldsymbol{m} - \boldsymbol{m}^{\mathrm{eq}}) + \Delta t(\boldsymbol{I} - \boldsymbol{\Lambda}/2)\overline{\boldsymbol{S}}, \tag{4}$$

where $\boldsymbol{m}$ and $\boldsymbol{m}^{\mathrm{eq}}$ are the equilibrium functions at the moment space via $\boldsymbol{M}f$ and $\boldsymbol{M}f^{\mathrm{eq}}$, respectively, and $\boldsymbol{I}$ is the unit

tensor. The forcing term vector in the moment space reads $\overline{\boldsymbol{S}} = \boldsymbol{M}\boldsymbol{S}'$, i.e.,[28]

$$\overline{\boldsymbol{S}} = \begin{bmatrix} 0 \\ 6v\cdot\boldsymbol{F} + \frac{\sigma|F_m|^2}{\psi^2\delta_t(\tau_e-0.5)} \\ -6v\cdot\boldsymbol{F} - \frac{\sigma|F_m|^2}{\psi^2\delta_t(\tau_\zeta-0.5)} \\ F_x \\ -F_x \\ F_y \\ -F_y \\ 2(v_xF_x - v_yF_y) \\ (v_xF_y + v_yF_x) \end{bmatrix}, \tag{5}$$

where σ is an parameter used to tune the mechanical stability condition, and the macroscopic velocity $\boldsymbol{v}$ can be obtained via $|\boldsymbol{v}| = \sqrt{v_x^2 + v_y^2}$. The density ρ can be calculated via

$$\rho = \sum_\alpha f_\alpha, \tag{6}$$

$$\rho\boldsymbol{v} = \sum_\alpha \boldsymbol{e}_\alpha f_\alpha + \frac{\delta_t}{2}\boldsymbol{F}, \tag{7}$$

where $\boldsymbol{F} = (F_x, F_y)$ is the total force acting on the fluid system. Noted that only the fluid-fluid force is adopted to present the intermolecular interaction force, which is given by[29,30]

$$\boldsymbol{F}(\boldsymbol{x}) = -G\psi(\boldsymbol{x})\sum_\alpha \omega(|\boldsymbol{e}_\alpha|^2)\psi(\boldsymbol{x}+\boldsymbol{e}_\alpha), \tag{8}$$

where ψ is the pseudopotential, which is expressed as $\psi(\boldsymbol{x}) = \sqrt{2(p_{\rm EOS} - \rho c_s^2)/Gc^2}$.[31,32] G is the interaction strength, and $\omega(|\boldsymbol{e}_\alpha|^2)$ is the weights, in which $\omega(1) = 1/3$ and $\omega(2) = 1/12$. The stream process is given as

$$f_\alpha(\boldsymbol{x}+\boldsymbol{e}_\alpha\Delta t, t+\Delta t) = f_\alpha^*(\boldsymbol{x}, t), \tag{9}$$

where $f_\alpha^* = \boldsymbol{M}^{-1}\boldsymbol{m}_\alpha^*$.

The temperature equation is solved by the finite-difference method in this work. The target temperature equation modified by Gong and Chen is written as[13]

$$\partial_t T + \nabla\cdot(\boldsymbol{v}T) = \frac{1}{\rho c_v}\nabla\cdot(\lambda\nabla T) + T\left[1 - \frac{1}{\rho c_v}\left(\frac{\partial p_{\rm EOS}}{\partial T}\right)_\rho\right]\nabla\cdot\boldsymbol{v}, \tag{10}$$

where λ is the thermal diffusivity, c_v represent the specific heat capacity at a constant volume. For simplicity, the right-hand side of Eq. (10) is denoted by $K(T)$. The classical fourth-order Runge–Kutta scheme is adopted for time discretization,[14,33]

$$T^{t+\delta_t} = T^t + \frac{\delta_t}{6}(h_1 + 2h_2 + 2h_3 + h_4), \tag{11}$$

where h_1, h_2, h_3, and h_4 reads

$$h_1 = K(T^t),\ \ h_2 = K\left(T^t + \frac{\delta_t}{2}h_1\right),$$

$$h_3 = K\left(T^t + \frac{\delta_t}{2}h_2\right),\ \ h_4 = K(T^t + \delta_t h_3). \tag{12}$$

For spatial discretization, the spatial gradient of a quantity ϕ is calculated by the following second-order isotropic difference schemes:

$$\partial_i\phi(\boldsymbol{x}) \approx \frac{1}{c_s^2\delta_t^2}\sum_\alpha w_\alpha\phi(\boldsymbol{x}+\boldsymbol{e}_\alpha\delta_t)e_{\alpha i}, \tag{13}$$

$$\nabla^2\phi(\boldsymbol{x}) \approx \frac{2}{c_s^2\delta^2 + t}\sum_\alpha w_\alpha[\phi(\boldsymbol{x}+\boldsymbol{e}_\alpha\delta_t) - \phi(\boldsymbol{x})], \tag{14}$$

where $w_0 = 4/9$, $w_{1-4} = 1/9$, and $w_{5-8} = 1/36$. The pseudopotential model for the flow field and the finite difference method for temperature field are coupled using the non-ideal equation of state (EOS) in the pseudopotential function $\psi(\boldsymbol{x}) = \sqrt{2(p_{\rm EOS} - \rho c_s^2)/Gc^2}$. The Carnahan–Starling (C–S) EOS is used:[31]

$$p_{\rm EOS} = \rho RT\frac{1 + b\rho/4 + (b\rho/4)^2 - (b\rho/4)^3}{(1-b\rho/4)^3} - a\rho^2, \tag{15}$$

where $G = -1$, $a = 0.4963(RT_c)^2/p_c$, $b = 0.1873RT_c/p_c$. In the present work, we choose $a = 1$, $b = 4$, $R = 1$. Thus, the critical temperature can be calculated to be $T_c = 0.09433$, the critical pressure is $p_c = 0.00441644$ and the critical density is $\rho_c = 0.13044$.

Note that all units in this work use lattice units of the LBM framework, as shown in Table 1.

Table 1. Basis parameter units (under the LBM system).

Name	Variable	Units	Dimensions
Length	δx	lu	L
Time	δt	ts	T
Mass	m	mu	M
Velocity	u	lu/ts	L/T
Pressure	p	mu/(ts^2·lu)	M/(T^{2}L)
Dendity	ρ	mu/lu^3	M/L^3
Viscosity	μ	lu^2/ts	L^2/T

3. Morphological measures

Morphology is a theory for analyzing spatial structure. It is developed on the basis of set theory, integral geometry, grid algebra and other disciplines, and it gradually becomes a commonly used image process technology. In recent years, the morphological analysis method has been applied to the field of physics such as phase separation and phase transition process of complex fluids. It has developed into a tool for effectively processing and extraction data and information from complex physical fields.[34,35]

In statistical physics, the Minkowski functional, also known as morphological measure, is a functional based on the morphological representation of geometric features of samples with different dimensions. In D-dimensional space, the number of the Minkowski function is $D+1$. For the two-dimensional (2D) space, the Minkowski functional mainly includes the coverage area A, the total length U of the boundary,

and the Gaussian integral curvature X that is also called Euler eigenvalues or Euler connectivity.[36] The main idea of the morphological analysis method based on the Minkowski functional aims to set a threshold for the physical quantities to be analyzed, such as temperature, density, and pressure threshold. The area above the threshold is white, and the area below the threshold is black. Therefore, almost all continuous patterns can be decomposed into small-scale patterns composed of white and black, also known as Turing patterns.[37]

For the D2Q9 lattice, the pixels can be imagined as regular quadrilateral plates centered on lattice nodes. The gray level can be associated with the local temperature $T(x)$ in each corresponding node. Due to the discrete lattice direction $\alpha = 0,\ldots,8$ and the lattice space of 1, there are $0 \leqslant T(\boldsymbol{x}), T_{\rm th} \leqslant T_{\rm max} = 9$. The first step in describing the morphological characteristics of the physical field is to set the threshold. The purpose of this paper is to explore the temperature distribution and thermodynamic effect of the collapsing bubble. Therefore, the temperature is used as a reference. The binary domain of the temperature threshold $T_{\rm th}$ can be defined as

$$\mathcal{P}(x,T_{\rm th}) = \begin{cases} 0, & T(x) < T_{\rm th}, \\ 1, & T(x) \geqslant T_{\rm th}, \end{cases} \tag{16}$$

where $\mathcal{P}(x,T_{\rm th})$ represents the binary image, $T(x)$ represents the gray level of the original image, and $T(x,T_{\rm th}) = 0$ represents the black pixel, corresponding to the 'low temperature area'. $T(x,T_{\rm th}) = 1$ is the white pixel, corresponding to the 'high temperature area'. The first Minkowski measure is the white coverage area $A(T_{\rm th})$, which defined as the total area of white pixels,

$$A(T_{\rm th}) = \frac{N_{T_{\rm th}}}{N} = \frac{1}{N}\sum_{x}\mathcal{P}(x,T_{\rm th}), \tag{17}$$

where $N_{T_{\rm th}}$ is the number of white pixels, and N is the total number of pixels.

The second Minkowski measure is the boundary length $U(T_{\rm th})$, which defined as the total length of the boundary connecting the white and black regions,

$$U(T_{\rm th}) = \frac{B_{T_{\rm th}}}{N} = \frac{1}{N}\sum_{T(x,T_{\rm th})=0}\sum_{\alpha=1}^{\alpha=8}\mathcal{P}(T+\boldsymbol{e}_{\alpha},T_{\rm th}), \tag{18}$$

where $B_{T_{\rm th}}$ is the total boundary length of the black and white regions. The third Minkowski measure is Euler eigenvalue $X(T_{\rm th})$ representing the difference between the number of white areas and the number of black areas,

$$X(T_{\rm th}) = N^{\rm w}_{T_{\rm th}} - N^{\rm b}_{T_{\rm th}}, \tag{19}$$

where the Euler eigenvalue cannot be obtained by calculated the binary function $\mathcal{P}(x,T_{\rm th})$ directly. In this paper, it is calculated by the connected domain recognition algorithm.

The collapse process of the bubble near the wall lacks periodicity, symmetry, spatial uniformity and obvious correlation, especially when the wall is complex and irregular. Through the morphological analysis method, we can more conveniently and intuitively observe the distribution and evolution of the temperature field in time and space, and quantitatively describe the heat transfer law of the flow field. Thus, a large amount of data generated during the collapse model of cavitation bubble near the wall can be processed and acquired, and the internal mechanism can be summarized.

4. Numerical simulation

As mentioned above, cavitation is an extremely complex process. Although many studies have been carried out successfully under the LB framework for simulating liquid-vapor phase change, the LB modeling of cavitation heat transfer phenomena is still in its infancy. Up to date, the modeling of the thermodynamics of cavitation bubble collapse near a complex wall has not been realized. In this section, we make an attempt to simulate the thermodynamics and dynamics of the cavitation bubble collapse near a fractal wall by using the proposed hybrid thermal LB model. In addition, the morphological analysis method is introduced to extract the characteristic behavior of the discrete LBM simulation results, and quantitatively describe the thermodynamic of cavitation bubble collapse near the fractal wall.

4.1. Simulation setup

The domain of the numerical model is $l_x \times l_y = 401 \times 401$. As shown in Fig. 1, the initial setting of the computational domain is such that a vapor bubble with radius 80 is in the center of the liquid, and the initial temperature is the corresponding coexistence temperature $T_\infty = 0.6T_{\rm c}$. The periodic boundary is defined in the x-axis, the Zou–He pressure boundary condition is applied at $y = l_y$, and the solid wall is applied at the bottom region.

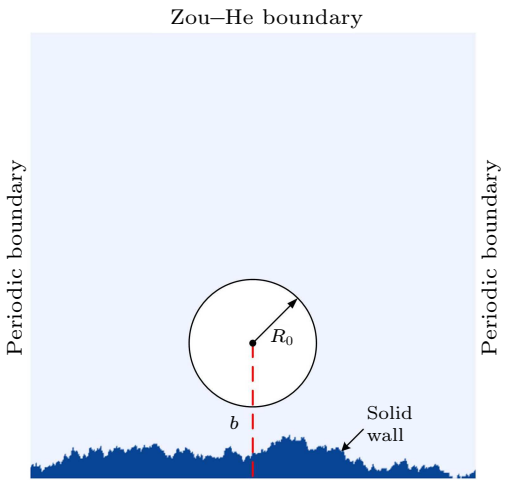


Fig. 1. Computational domain.

In this work, the 2D model of the fractal solid wall with the characteristics of natural rock wall is transformed by the fracture synthesis software SynFrac.[38] The fractal dimension of the curve is used to describe the complexity of the curve, and the value range is between 1 and 2. Li *et al.*[39] proposed a 'sliding window' method to modify the fractal dimension model of the curve. The core is to set a certain scale in advance. A sliding template is formed to divide the object space by overlapping or connecting with each other. The modified model is applied to the model of cavitation bubble collapse near the fractal wall, and the schematic diagram is shown in Fig. 2. The chord length L of the dotted line is obtained by calculating the first coordinate of the solid wall, and then the sliding window method is used to calculate the scale number. The scale polyline in this model is a sliding window, and its length is a grid unit distance d. The fractal dimension D of the wall can be obtained by covering the scale polyline to the solid wall:

$$D = \frac{\ln N(d)}{\ln(L/d)}, \tag{20}$$

where $N(d)$ is the scale number. L is the length of the straight line, which connects the starting and ending points of the curve. Based on this, the different fractal dimensions can be calculated and introduced into the numerical model.

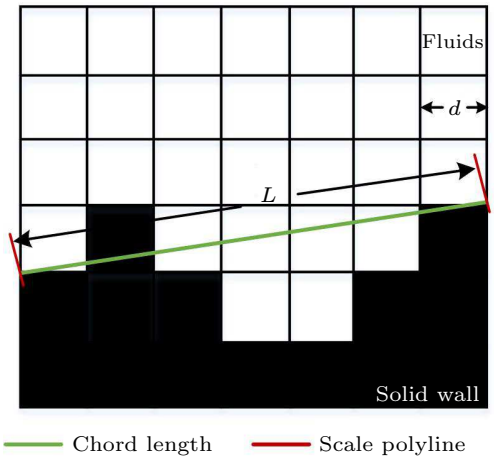


Fig. 2. Schematic diagram of the fractal dimension calculation model.

In addition, the standard bounce-back boundary condition is used to deal with the bottom fractal wall. The grid of bounce-back boundary layer is adjacent to the solid boundary. Table 2 shows the basic idea of boundary processing flow.

In Table 2, LabelArray $(x_1 + e_{\alpha\delta_t})$ denotes the value of the label array corresponding to the current fluid particle along its motion direction to the next node. LabelArray $(x_1 + e_{\alpha\delta_t}) = 0$ indicates that the node is a fluid node, otherwise it is a solid node. Here f_α represents the distribution function of particles moving towards the bounce-back boundary, and $f_{-\alpha}$ is the distribution function of particles moving in the opposite direction to f_α.

It should be noted that both the complexity of the solid wall and the distance between cavitation bubble and the wall impact the bubble collapse process. In order to study the effect of complexity on the numerical model, it is necessary to study the collapse process of the bubble under the condition that the distance between the bubble and the wall remains unchanged based on the idea of the control variable research method. In the previous works,[6,7] we used the dimensional position offset parameter $\lambda = b/R_0$ to measure the distance between the bubble and the flat solid wall (the fractal dimension $D = 1$). In the present work, an 'equivalent distance' λ_e is introduced to define the distance between the bubble and the bottom wall. When the first collapse time obtained by simulating the fractal wall model is equal to the first collapse time of the model of the flat solid wall, the λ in the flat wall model can be considered to describe the distance between the bubble and the fractal wall. The equivalent distance λ_e can be regarded as $\lambda_e = \lambda$. Furthermore, the mechanism between the cavitation thermal effect and the fractal wall can be explored.

Table 2. Boundary processing flow of the fractal geometric solid wall.

Input: Marking the array LabelArray $(x_1 + e_{\alpha\delta_t})$
Output: Distribution functions
1. if LabelArray $(x_1 + e_{\alpha\delta_t}) = 1$ then
2. $f_{-\alpha}(x_1, t+\delta_t) = f_\alpha(x,t)$;
3. else
4. $f_{-\alpha}(x_1, t+\delta_t) = f_\alpha(x_1, t+\delta_t, t+\delta_t)$;
5. end if;
6. return $f_{-\alpha}(x_1, t+\delta_t)$

4.2. Dynamic model verification and analysis

In order to verify the effectiveness and feasibility of the near-fractal solid wall collapse numerical model of a cavitation bubble, this paper compares the experimental data with the LBM simulation results to determine whether the shape evolution processes described by the two methods are consistent. The model can introduce fractal solid walls with arbitrary geometric features. Through 3D printing technology, the same solid solid wall as the numerical model (surface complexity $D = 1.1389$) can be constructed. Figure 3 shows the comparison between the numerical results and the experimental data. Figure 3(a) shows the shape evolution process during the collapse of the cavitation bubble captured by a high-speed camera. The cavitation bubble radius $R = 0.5$ mm, and the relative distance between the cavitation bubble and the wall is 1.6. Figure 3(b) is the pressure and velocity distribution cloud diagram obtained by the LBM numerical simulation. In the simulation, the cavity radius is set to $R = 0.80$ lu, and the position parameter is set to $\lambda_e = 1.6$. In comparison of the two sets of figures, it is found that the cavitation bubble shape evolution process obtained by the LBM simulation is consistent with the experimental results. After preliminary verification,

this numerical model can be used to simulate the collapse process of cavitation bubbles near any fractal solid wall, to study the evolution of its shape, density field, pressure field and velocity field, and to explore the microscopic mechanism of their interaction.

The dynamic mechanism is investigated by the evolution of the pressure and velocity field. Note that we focus on the key regions in the flow field. The pressure field phase diagram only shows the flow field near the solid wall of the bubble. Initially, cavitation bubble shrinks inward under the action of Δp, and the pressure of the fluid near the solid wall becomes lower, which makes the bottom curvature of the bubble larger. At $t = 400$, the bubble is elongated under the impacting effect of the solid wall. Meanwhile, it is observed that the deformation of the bubble is not symmetrical due to the surface of the solid wall is concave-convex, disordered and uneven. The bubble boundary near the convex of the wall deforms faster and the profile changes more obviously. At $t = 500$, a depression is formed at the top of the bubble, indicating that there is a relatively concentrated high-pressure region above the bubble, and the fluid velocities on the top region increase to form a primary micro-jet. Subsequently, the top concave degree of the bubble increases (at $t = 560$), and the collapse velocity also increases. The micro-jet is about to hit the bubble when the first collapse occurs (at $t = 620$). In the meantime, it is found that the direction of the micro-jet does not penetrate the bubble vertically but points on the lower side of the wall. As a result, the left side of the bubble is more impacted by the micro-jet and begins to collapse firstly. A toroidal bubble is formed after the first collapse. On the 2D level, the toroidal bubble is divided into two parts with different shapes and sizes. At $t = 700$, it can be seen that the shock wave from the first collapse diffuses rapidly and hits the fractal solid wall downward to produce a high-pressure region. Due to the influence of the fractal wall height, the deformation is asymmetric, and the left side of the toroidal bubble collapses first and forms a radial pressure wave with the propagation trend at the collapse point. The right side of the bubble finishes the second collapse driven by the upper and lower micro-jet to form a shock wave, which acts on the solid wall. At the moment, the flow field includes the shock wave rebounded from the wall after the first collapse, the shock wave generated by the left toroidal bubble and the right toroidal bubble collapses for the second time. The original simple wave system is transformed into a complex wave system. Two vortices are generated at the final collapse point and diffuse to the surrounding fluid until they disappear.

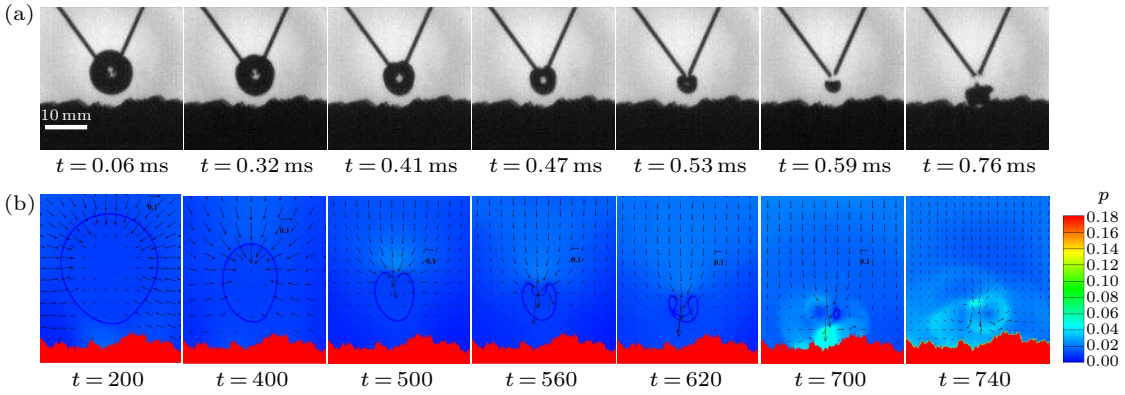


Fig. 3. Pressure and velocity field of the bubble collapse near the fractal solid wall.

The simulation results describe the whole collapse process of the bubble, including internal contraction, deformation, jet formation, the first collapse, and the second collapse stages. It can be seen that the fractal wall has a significant impact effect on the collapse process, and the reflection path of shock wave is obviously influenced by the geometry and fractal dimension of the wall.

4.3. Temperature field and morphological analyses

Based on the dynamic analysis of pressure and velocity field in Subsection 4.3, the thermodynamic essence of the bubble collapse near the fractal solid wall is further analyzed. Figure 5 shows the temperature distribution pattern during the collapse process. Initially, the fluid temperature is uniform, and the wall temperature is lower than the ambient temperature and constant.

When the bubble begins to shrink, it can be seen from the distribution of the pressure and velocity field shown in Fig. 3(b). The velocity of the fluid in the upper region of the bubble increases, resulting that the temperature in the top region of the bubble-liquid interface rises. With the emergence of the top micro-jet, the temperature at the interface further increases with the depression degree of the bubble, as shown in Figs. 4(a)–4(c). Meanwhhile, Fig. 3(b) explains that the bubble is elongated longitudinally due to the existence of the solid wall. The smaller the vertical distance between the bubble and the fractal wall, the faster the fluid velocity of this region, and

the higher the temperature at the corresponding vapor-liquid interface. Figure 4(d) shows the temperature distribution image of the bubble at the first collapse. It can be observed that the temperature of the micro-jet is non-equilibrium. The reason is that the depression and collapse process is dominated by the external pressure. Different from the flat wall model, the direction of the top micro-jet is not single vertical points to the wall due to the uneven and fractal wall. The micro-jet shock converges and collides in the depression region, resulting in the unbalanced temperature distribution in this region. Figure 4(f) shows that the bubble turns into a toroidal bubble after being broken down by the micro-jet, and the bubble profile of the left part has completely disappeared due to the higher external fluid velocity and pressure. The shock wave with high-temperature hits the bottom wall, and the disconnected high temperature regions gradually converge. The visible outline disappears completely during the second collapse [Fig. 4(e)]. There are multiple pressure waves interacting and colliding in the flow. The heat energy hits the wall with the pressure waves, and a high temperature vortex occurs at the collapse point [Figs. 4(g) and 4(h)]. Eventually the entire fluid region reaches equilibrium as the shock wave spreads along the surface of the fractal solid wall.

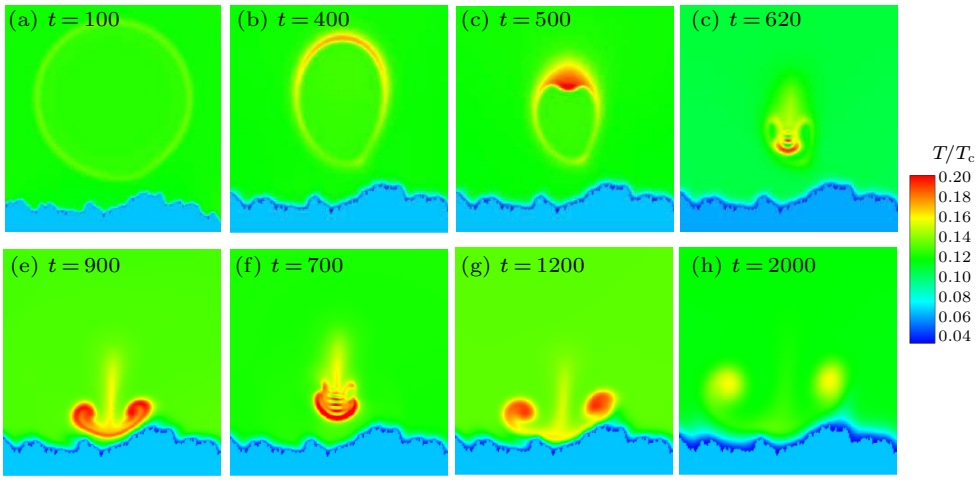


Fig. 4. Temperature field of the bubble collapse near the fractal solid wall.

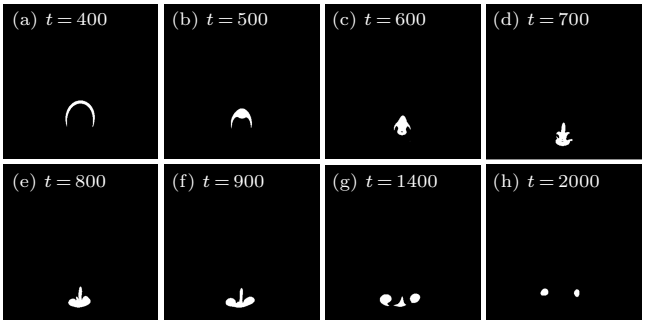


Fig. 5. Binary of temperature ($T_{th} = 0.8T_c$).

During cavitation bubble collapse near the fractal wall, its morphological profile is no longer symmetrical, specially the distribution of high temperature regions caused by shock waves becomes diverse and disordered. In order to explore the temperature distribution and thermodynamic characteristics in the collapse process, the above simulation process is quantitatively analyzed by the morphological analysis method based on the Minkowski functional. First, the pattern (structure) features corresponding to the above simulated temperature field are extracted. Figure 5 shows the temperature binary image at different time steps under the temperature threshold $T_{th} = 0.8T_c$. The white region corresponds to the 'high temperature' region, and the black corresponds to the 'low temperature' region, where the high temperature and the low temperature are relative to the chosen temperature threshold. Using the binary image, the temperature characteristics of fluids in different thresholds can be clearly observed.

Figure 7 is a group of morphological analysis results of the evolution of three morphological parameters with time step during thermodynamic process. It can be seen from Fig. 7(a) that the curve shows a rapid growth trend after a period of time. It is demonstrated that the high-temperature regions appear in the flow field and increase gradually. Then, the curve has a briefly decline process, which corresponds to the stage from depression in the top region of the bubble to collapse. It indicates that the change of thermodynamic process is slow, and the area of the high-temperature region decreases. After the first collapse, the curve rises sharply again and reaches the peak, indicating that the high-temperature shock wave generated by the first collapse leads the area of the high-temperature region to increase. After a brief decline, it rises again under the influence of the high-temperature shock wave from the second collapse, then the curve shows a downward trend. At the same time, it is observed that the curve is undulating due to the collision of multiple shock waves in the fluid, which may generate sporadic white pixels. The white pixel can be regarded as 'hot

spot', resulting in burrs and non-smoothness in the curve.

Figure 6(b) shows the evolution of the boundary length of the white area. It can be seen that the trend of the curve is basically consistent with the curve in Fig. 6(a), which indicates the area A. The curve between the first collapse and the second collapse changes violently due to the presence of multiple discontinuous high-temperature regions (white pixels) at the moment, and the boundary length increases and decreases rapidly with their appearance and disappearance. Figure 6(c) reflects the connectivity of the high and low temperature regions in the binary diagram. The larger the number, the worse the connectivity, and the corresponding high-temperature region becomes smaller and scattered. The value of X increases sharply at the beginning and becomes 1 after a rapid oscillation transformation, indicating that the connectivity of the high-temperature region is good. Then, the X changes into 1 again after a sharp increase and decrease transformation, which illustrates that the thermodynamic process changes violently after the first collapse. The curve of X becomes 1 again after the second collapse and becomes 0 finally. It is observed that the oscillation alternating process of the curve after the second collapse is gradually smoother than that of the first collapse. By using the three measurement curves of Minkowski functional, the key stages of the bubble collapse can be distinguished, and the thermodynamic characteristics can be analyzed. It also demonstrates the effectiveness of morphological analysis method in analyzing the thermodynamic process of the bubble collapse.

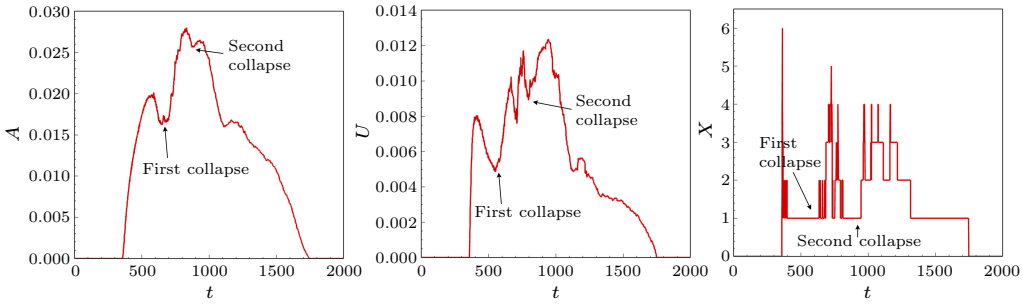


Fig. 6. Morphological analysis of the thermodynamic process of cavitation bubble collapse.



Fig. 7. Binary temperature diagrams of four similar thermodynamic process at $t_s = 700$: (a) $T_{th} = 0.8T_c$, (b) $T_{th} = 0.9T_c$, $T_{th} = T_c$, $T_{th} = 1.1T_c$.

4.4. Thermodynamic similarity at different temperature thresholds

The temperature distribution characteristics of the flow field can be determined by setting the size of the temperature threshold. The temperature binary diagram under different temperature thresholds at $t = 700$ ts is given in Fig. 7. It can be intuitively seen that the parts of the high-temperature region corresponding to different thresholds are different. The higher the threshold, the less the white area is displayed.

Figure 8 shows a set of morphological analysis results for the evolution of three morphological measures with time step t in the thermodynamic process of cavitation bubble. It can be seen from Fig. 8(a) that the higher the T_{th}, the smaller the value of A, and the shorter the time of appearance. For example, when $T_{th} = 1.1T_c$, the area of high-temperature region $A = 0$ at $t = 700$ ts, which corresponding to the stage before and after the first collapse of the bubble. It indicates that the thermodynamic process evolves violently, and many high-temperature regions are generated in the flow field. The value U in Fig. 8(b) represents the size of the boundary length. As the threshold increases, the total length of the boundary between the black and white area decreases gradually. The trend of U is roughly the same as that of the curve of A, which initially increases to the peak value and decreases to zero. However, the green curve is higher than the red curve (the part circled in the figure) when $t = 800$ ts. Corresponding to the Euler characteristic number X in Fig. 8(c), $X = 6$ of the green curve at $t = 800$ ts, while $X = 2$ of the red curve. It indicates that the high-temperature region is more dispersed, and the boundary length is larger when $T_{th} = 0.9T_c$ (the green curve). The high-temperature region is larger and concentrated, the boundary length contacting the low-temperature region is less when $T_{th} = 0.8T_c$ (the red curve), illustrating that the high and low temperature regions have better connectivity.

The morphological analysis results in Fig. 9 are obtained by changing position offset parameter λ_e to 1.6. The similar result of Fig. 8 also appears in the part of the black circle in Fig. 9(b). It can be seen that before and after the first collapse ($t = 620$ ts) and the second collapse ($t = 800$ ts), the area of the white region under the threshold $T_{th} = 0.9T_c$ is small. Due to the large and scattered distribution of high-temperature region when $T_{th} = 0.9T_c$, the value of the total boundary length U connecting with the black is larger than that of U under

$T_{\rm th} = 0.8T_{\rm c}$. It can be inferred that the boundary length does not necessarily increase with the threshold, and each threshold has different thermodynamic characteristics.

The above three morphological parameters A, U, and X describe the characteristics of temperature binary diagram from three relatively independent views. However, the dimensions of the three parameters are different, and their values are not comparable. Therefore, in order to better describe the morphological characteristics of thermodynamics, a phase space is established based on the three independent morphological parameters to study the morphological characteristics of the pattern in a phase space.

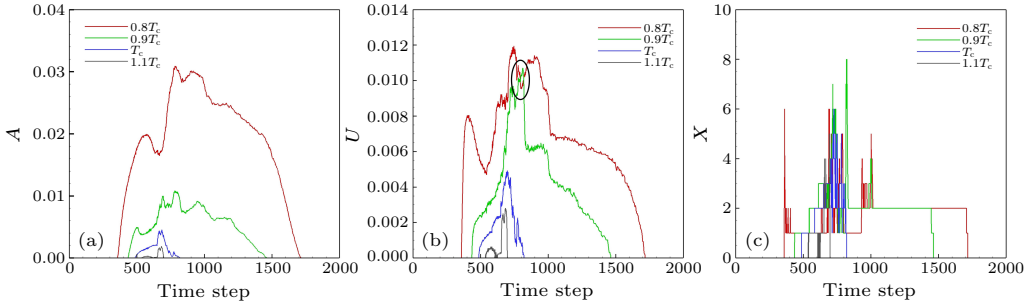


Fig. 8. Morphological analysis of thermodynamic process under different $T_{\rm th}$ ($\lambda_{\rm e} = 1.4$, $D = 1.03444$).

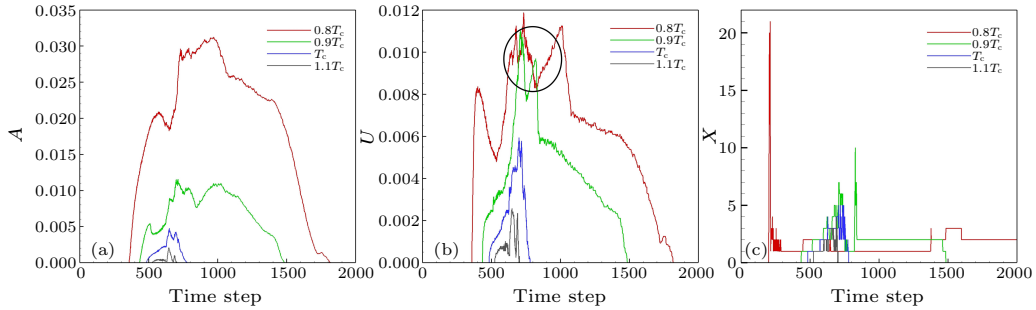


Fig. 9. Morphological analysis of thermodynamic process under different $T_{\rm th}$ ($\lambda_{\rm e} = 1.6$, $D = 1.03444$).

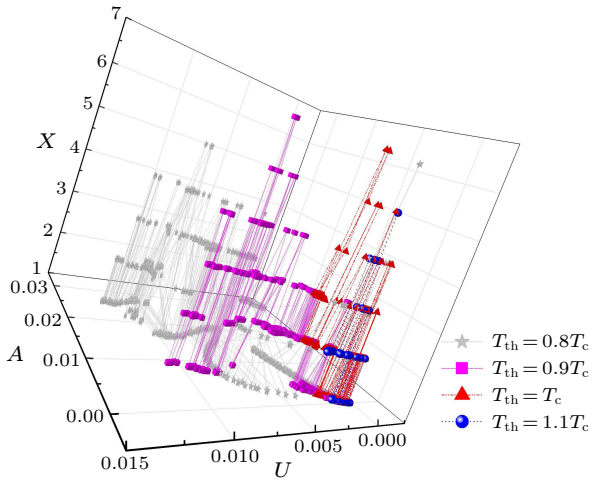


Fig. 10. Morphological analysis in the A–U–X space.

Figure 10 shows a schematic diagram of the thermodynamic process of the bubble collapse in the A–U–X space, where a point represents a measurement time point. The higher the degree of curve overlap, the higher the similarity of the thermodynamic process. It can be seen that the curve of $T_{\rm th} = 0.8T_{\rm c}$ hardly coincides with the other three curves, while the curves of $T_{\rm th} = T_{\rm c}$ and $T_{\rm th} = 1.1T_{\rm c}$ are relatively close, indicating that the two thermodynamic processes have high similarity.

4.5. Thermodynamic similarity under different fractal dimensions

The similarity of thermodynamic process of the bubble collapse near the solid wall under different fractal dimensions is studied by adjusting the fractal dimension of the wall. The other original system parameters such as initial temperature and pressure remain unchanged.

Figure 11 shows a group result of morphological measurement curves when the temperature threshold $T_{\rm th} = 1.1T_{\rm c}$. It can be seen from Fig. 11(a) that the larger the fractal dimension D, the later the high-temperature region of flow occurs. It is also observed that the curves of $D = 1.0344$ and $D = 1.0821$ grow slowly initially, indicating that a small area of high-temperature region occurs in the system. The curve of $D = 1.1389$ grows faster, which illustrates that the area of high-temperature region is wide and concentrated at the moment. In the late stage of the collapse, the three curves all experience the peak and gradually decrease to 0, indicating that the high-temperature region changes from aggregation to dispersion distribution, and finally disappears with the end of the collapse. The boundary length U is shown in Fig. 11(b). The growth trend of the curve U is close to the curve of A,

that is, the total boundary length of the high-temperature region increases and decreases with the high-temperature area. From the perspective of Euler characteristic coefficient X [Fig. 11(c)], the curve of X generally shows the topological change of high-temperature region. The greater the fractal dimension, the larger the maximum Euler characteristic coefficient X, illustrating that the high-temperature region is dispersed largely at this moment.

By comparing the curves under different fractal dimensions, it can be inferred that the increase of the complexity of the solid wall not only affects the thermodynamic behaviors of the bubble collapse, delays the occur time of the high-temperature region, but also makes the topological change of high-temperature region more intense. The morphological characteristic curve in the A–U–X space corresponding to the above process is shown in Fig. 12. It can be seen that the curve path and coincidence of $D = 1.0344$ and $D = 1.0821$ are very close, indicating that the thermodynamic processes of the two fractal dimensions are similar.

In summary, various characteristic structures will appear in the temperature field of cavitation bubble collapse near the fractal wall. The research elucidates that the complexity of the solid wall is one of the main factors affecting the thermodynamic characteristics. Due to the existence of the complex solid wall, the bubble no longer collapses in spherical symmetry, and the distribution positions of high-temperature region become more and more scattered. In the meantime, it is found that different fractal dimensions of solid wall may show strong similarity. Therefore, the mechanism of its various characteristics and laws is worthy of in-depth study, and it can be reasonably used in engineering applications further.

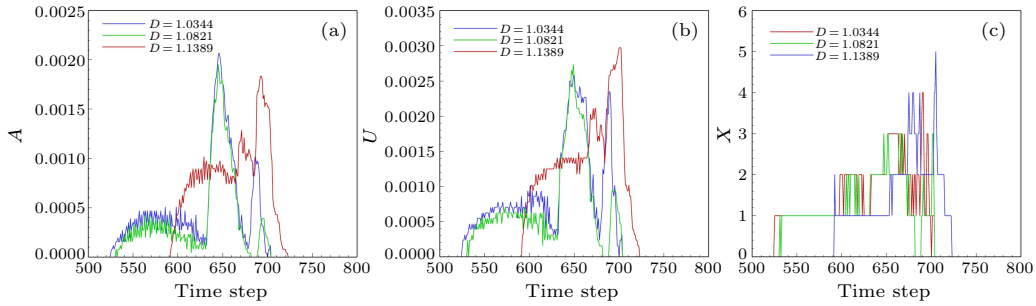


Fig. 11. Morphological analysis for the thermodynamic process under different fractal dimensions.

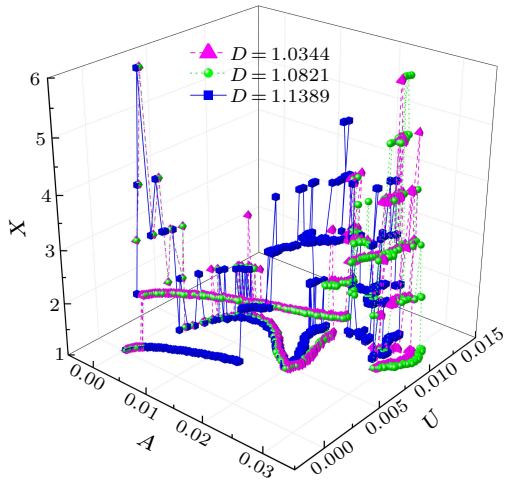


Fig. 12. Minkowski description in the A–U–X space.

5. Conclusion

In this paper, a hybrid LBM and morphological analysis based on the Minkowski functional are mainly used to establish the thermodynamic model of cavitation bubble collapse near the fractal wall. By introducing complex geometric boundaries conforming to the characteristics of natural walls, the physical model with fractal and irregular geometry is constructed. The complexity degree of the fractal geometric wall is described by the fractal dimension. Meanwhile, the concept of equivalent distance is introduced to describe the distance between the bubble and the solid wall. The simulation results of pressure and velocity field are analyzed to verify the feasibility of the hybrid LBM. The thermodynamic process of the bubble collapse is further analyzed, and the LBM data are processed to obtain three measurement curves of the Minkowski functional. The quantified curve can describe the stage of the bubble collapse processes and the complex and changeable thermodynamic characteristics. It demonstrates the effectiveness of using the morphological analysis method to analyze the thermodynamic process of the bubble collapse near the fractal wall. Finally, the relationship between temperature threshold and thermodynamic characteristics is analyzed. By choosing different thresholds, the distribution characteristics of high-temperature region in the thermodynamic process of the bubble collapse can be obtained, and the influence of the fractal dimension on the similarity of thermodynamic process is discussed. The results show that the temperature field patterns with different complexity of the wall may show strong similar morphology and evolution process.

The two methods used in this paper can study many redundant and irregular information of complex physical field

hierarchically and quantitatively from different perspectives. The present work discusses the heat transfer mechanism of the bubble collapse near the fractal geometric wall, which provides a theoretical basis for thermodynamic research in the applied field where the cavitation phenomenon actually occurs. In addition, the morphological analysis method is tentatively introduced into the analysis of the thermodynamic process of the bubble collapse near the fractal wall, and the results illustrate that the morphological analysis can be used as an optional and potential tool for information acquisition and processing in the research field of complex multiphase flow physical field. In the future, it can be extended to the numerical model of arbitrary complex geometric wall.

Acknowledgments

This work was supported by the National Natural Science Foundation of China (Grant Nos. 11874140 and 12174085), Basic Science (Natural Science) Research Project for the Universities of Jiangsu Province (Grant No. 23KJD140002), and the Natural Science Foundation of Nantong (Grant No. JC2023081).

References

[1] Brennen C E 2005 *Fundamentals of Multiphase Flow* (New York: Cambridge University Press) p. 19
[2] Koch M, and Lechner C, Reuter F K and Lauterborn W 2016 *Comput. Fluids* **126** 71
[3] Guo X S, Cai C, Xu G, Yang Y, Tu J, Huang P T and Zhang D 2017 *Ultrason. Sonochem.* **39** 863
[4] Kyriazis N, Koukouvinis P and Gavaises M 2017 *Int. J. Multiphase Flow* **93** 158
[5] Yang Y, Shan M L, Kan X F, Duan K J, Han Q B and Juan Y 2023 *Heliyon* **9** e20532
[6] Shan M L, Yang Y, Zhao X M, Cheng Y and Han Q B 2021 *Chin. Phys. B* **30** 044701
[7] Yang Y, Shan M L, Kan X F, Shangguan Y Q and Han Q B 2020 *Ultrason. Sonochem.* **62** 104873
[8] Yang Y, Shan M L, Han Q B and Kan X F 2020 *Chin. Phys. B* **30** 024701
[9] Liu Y and Peng Y 2021 *J. Mar. Sci. Eng.* **9** 219
[10] Peng H N, Zhang J, He X L and Wang Y 2020 *Compu. Fluids* **217** 104817
[11] Leemput P V, Vandekerckhove C, Vanroose W and Roose D 2007 *Siam Journal on Multiscale Modeling and Simulation* **6** 838
[12] Lallemand P and Luo L S 2008 *Int. J. Mod. Phys. B* **17** 41
[13] Shuai G and Ping C 2012 *Int. J. Heat Mass Tran.* **55** 4923
[14] Li Q, Kang Q J, Francois M M, He Y L and Luo K H 2015 *Int. J. Heat Mass Tran.* **85** 787
[15] Liu Y and Peng Y 2020 *Energies* **13** 4398
[16] Shan M L, Zhu C P, Zhou X, Cheng Y and Han Q B 2016 *J. Hydrodyn.* **28** 442
[17] Dular M and Coutier-Delgosha O 2013 *Journal of Fluid Mechanics* **735** 44
[18] Chahine G L, Kapahi A, Choi J K and Hsiao C T 2016 *Ultrason. Sonochem.* **29** 528
[19] Serra J 1982 *Biometrics* **39** 536
[20] Mecke K 1996 *Phys. Rev. E* **53** 4794
[21] Gan Y B, Xu A G, Zhang G C, Li Y J and Li H 2011 *Phys. Rev. E* **84** 046715
[22] Xu A G, Zhang G, Ying Y, Zhang P and Zhu J 2010 *Phys. Scr.* **81** 055805
[23] D'Humieres D, Ginzburg I, Krafczyk M, Lallemand P and Luo L S 2002 *Phil. Trans. R. Soc. A* **360** 437
[24] Chai Z H and Shi B C 2020 *Phys. Rev. E* **102** 023306
[25] Chai Z H, Shi B C and Guo Z L 2016 *J. Sci. Comput.* **69** 355
[26] Guo Z, Shi B and Zheng C 2002 *Int. J. Numer. Methods Fluids* **39** 325
[27] Chai Z H and Zhao T S 2012 *Phys. Rev. E* **86** 016705
[28] Li Q, Luo K H and Li X J 2013 *Phys. Rev. E* **87** 053301
[29] Shan X W and Chen H D 1993 *Phys. Rev. E* **47** 1815
[30] Shan X W and Chen H D 1994 *Phys. Rev. E* **49** 2941
[31] Yuan P and Schaefer L 2006 *Phys. Fluids* **18** 042101
[32] Shan X W 2006 *Phys. Rev. E* **73** 047701
[33] Li Q, Yu Y, Zhou P and Yan H J 2018 *Appl. Therm. Eng.* **132** 490
[34] Zhang Y D, Xu A G, Zhang G C, Gan Y B, Chen Z H and Succi S 2019 *Soft Matters* **15** 2245
[35] Chen F, Xu A G, Zhang Y D and Zeng Q K 2020 *Phys. Fluids* **32** 104111
[36] Arns C H, Mecke J, Mecke K and Stoyan D 2005 *Eur. Phys. J. B* **32** 397
[37] Xu A G, Song J, Chen F, Xie K and Ying Y 2021 *Chin. J. Comput. Phys.* **38** 631 (in Chinese)
[38] Ogilvie S R, Isakov E and Glover P 2006 *Earth Planet. Sci. Lett.* **241** 454
[39] Li B, Tong J, Xiao X, Zhang J, Xu Y, Wang W, Yan F, Yang C and Chen X 2010 *Mapping Science* **35** 41 (in Chinese)